Localized to Itinerant Electronic Transitions in Transition-Metal Oxides with the Perovskite Structure

J. B. Goodenough* and J.-S. Zhou

Center for Materials Science & Engineering University of Texas at Austin, Austin, Texas 78712-1063

Received April 13, 1998. Revised Manuscript Received June 16, 1998

The transition from localized to itinerant electronic behavior is shown to be first-order. In a perovskite, segregation into localized-electron and itinerant-electron phases can be accomplished by cooperative atomic displacements. $Sr_{1-x}Ca_xVO_3$ and $La_{1-x}Nd_xCuO_3$ illustrate single-valent perovskites that exhibit localized-electron fluctuations in an itinerant-electron matrix on approaching the Mott−Hubbard transition, and $CaFeO_3$ and $NdNiO_3$ form charge-density waves with MO complexes or itinerant-electron slabs alternating with localized-electron states.

Contents

I. Introduction

This review addresses crossovers from localized to itinerant electronic behavior in AMO_3 stoichiometric oxides with the perovskite structure that contain a single first-long-period transition-metal atom M. The larger A atoms in these structures are lanthanide or yttrium and/or alkaline-earth atoms.

The perovskite structure allows extensive cation substitutions as well as the introduction of vacancies at any atomic site; it is also able to adapt to a mismatch of the equilibrium A−O and M−O bond lengths. This flexibility allows extensive chemical substitution and/or deviation from oxygen stoichiometry. This review is restricted to stoichiometric and single-valent MO_3 arrays in which M is a transition-metal atom. Appropriate substitutions of isovalent A cations of different size are used to change hexagonal polytypes or to modulate the bending angle ϕ of the dominant $(180° - \phi)$ M−O−M interatomic interactions within a pseudocubic MO_3 array. Modulation of the angle ϕ and/or the oxidation state of the MO_3 array can, in several cases, induce a transition from localized to itinerant 3d electrons at first-long-period transition-metal atoms M. Substitution of an aliovalent A cation also changes the oxidation state of the MO_3 array from single-valent to mixed-valent, but in this review we focus attention on single-valent MO_3 arrays.

An adequate description of a localized-to-itinerant electronic crossover is confronted with the need to consider not only strong electron correlations and spin−spin interactions, but also strong electron interactions with oxygen atom vibrations. Where the latter interactions result in a static charge-density wave (CDW) or a cooperative Jahn−Teller (J−T) deformation, the characteristics of the interactions can be clarified by a diffraction experiment. However, experiments designed to sort out the characteristics of the electron−lattice interactions in a dynamic situation are confronted by time scales $\tau < 10^{-12}$ s, which are too short for a conventional diffraction experiment. Nevertheless, there is mounting indirect evidence that dynamic electron−lattice interactions are dominant if J−T or pseudo-J−T deformations can occur at some of the M atoms of the MO_3 arrays, and fast experimental probes are beginning to provide more direct information on how these interactions organize the electronic and vibrational components into vibronic states within a three-dimensional MO_3 array or a two-dimensional MO_2 sheet in an intergrowth structure.

We introduce structural and electronic considerations needed to interpret the properties of the transition-metal oxides with perovskite-related structures, including the cooperative oxygen displacements that are encountered, before we present relevant data for several systems that approach or undergo a transition from localized to itinerant electronic behavior.

II. Structural Considerations

A. Tolerance Factor. Figure 1a shows the ideal AMO_3 cubic-perovskite structure. Matching of the equilibrium A−O and M−O bond lengths would correspond to a geometrical tolerance factor

$$t \equiv (\text{A}-\text{O})/\sqrt{2}(\text{M}-\text{O}) = 1 \qquad (1)$$

where the equilibrium bond lengths are normally calculated for room temperature and atmospheric pressure from the sums of ionic radii; the radii have been obtained from X-ray diffraction data and are available in tables.[1] In the oxygen-stoichiometric perovskites to be discussed, the MO_3 array contains a single M atom and no vacancies, but the *t* factor and the oxidation state of the MO_3 array are varied by introducing A cations of

10.1021/cm980276u CCC: $15.00
Published on Web 10/02/1998

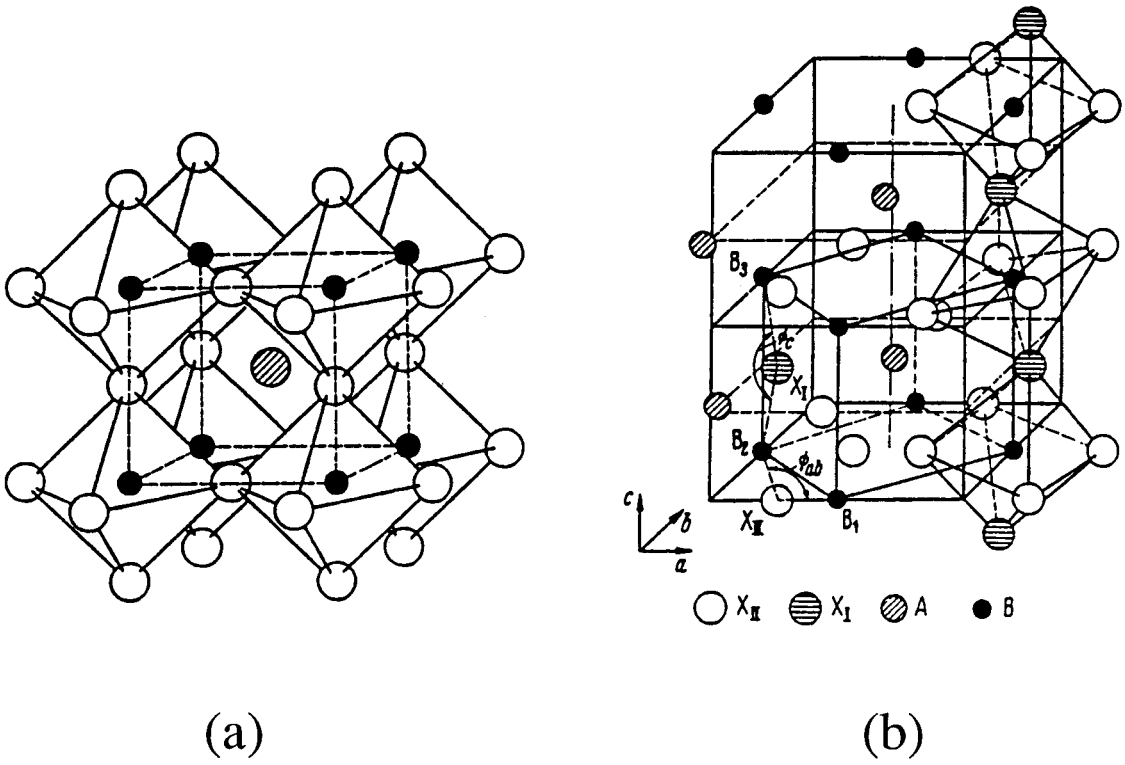

Figure 1. (a) The ideal cubic and (b) the orthorhombic AMO_3 perovskite structure.

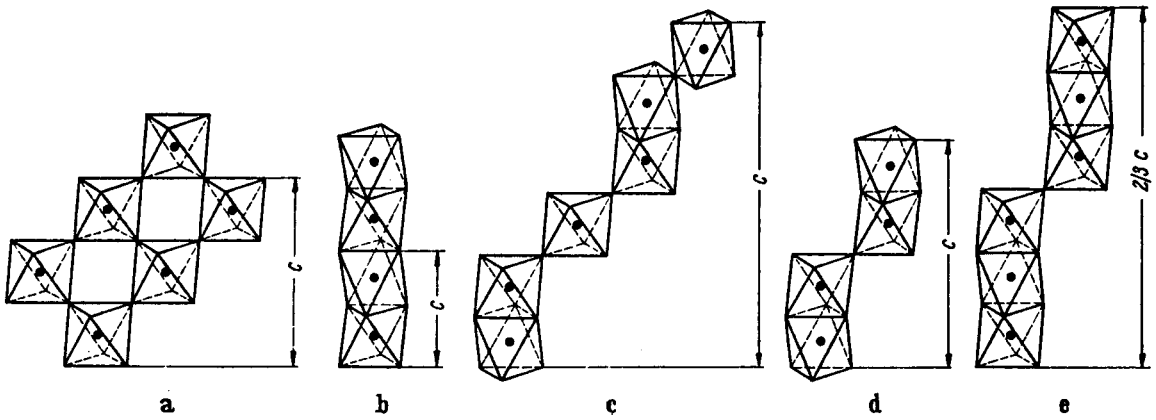

Figure 2. Perovskite polytypes: (a) cubic, (b) hexagonal 2H, (c) hexagonal 6H, (d) hexagonal 4H, and (e) rhombohedral 9R. Octahedral sites share corners in cubic stacking, faces in hexagonal stacking of close-packed AO_3 planes.

different size and charge. With mixed A cations and a mixed valence on the MO_3 array, averaged equilibrium bond lengths are used in eq 1.

At $t < 1$, the M−O bonds are under compression and the A−O bonds are under tension. The lattice relieves these stresses by cooperative rotations of the corner-shared MO_6 octahedra about a cubic crystallographic axis, which bend the M−O−M bond angles from 180° to (180° − ϕ) and reduce the number and length of the shortest A−O bonds.[2] These cooperative rotations also reduce the crystal symmetry: rotations about a [001] axis give tetragonal symmetry $I4/mcm$, those about a [111] axis give rhombohedral ($R\bar{3}c$) symmetry, those about a [110] axis give orthorhombic ($Pbnm$ or $Pnma$) symmetry (Figure 1b), and those about a [101] axis give orthorhombic ($Imma$) symmetry.[3] The most common structures are rhombohedral and orthorhombic. Phase transitions involving oxygen-atom displacements away from one M atom near neighbor toward the other are superimposed on these cooperative rotations.

At $t > 1$, the A−O bonds are under compression and the M−O bonds are under tension; these stresses are relieved by a change from cubic to hexagonal stacking of the AO_3 close-packed planes of Figure 1a.[4] Hexagonal stacking introduces columns of face-shared MO_6 octahedra that are bound to one another only by A−O bonds, which eliminates any problem with bond-length mismatch. However, stronger electrostatic $M^{m+} - M^{m+}$ repulsive interactions occur across shared octahedral-site faces, so the perovskite structure changes with increasing $t > 1$ from all-cubic to all-hexagonal stacking of AO_3 planes by the series of hexagonal polytypes illustrated in Figure 2. In the 6H and 4H structures, pairs of face-shared octahedra allow *c*-axis displacements of the M^{m+} cations from the centers of their octahedra to reduce the electrostatic repulsions between them; in the 9R polytype, units of three face-shared octahedra allow the outer two M^{m+} cations to be displaced along the *c*-axis. More complex polytypes may

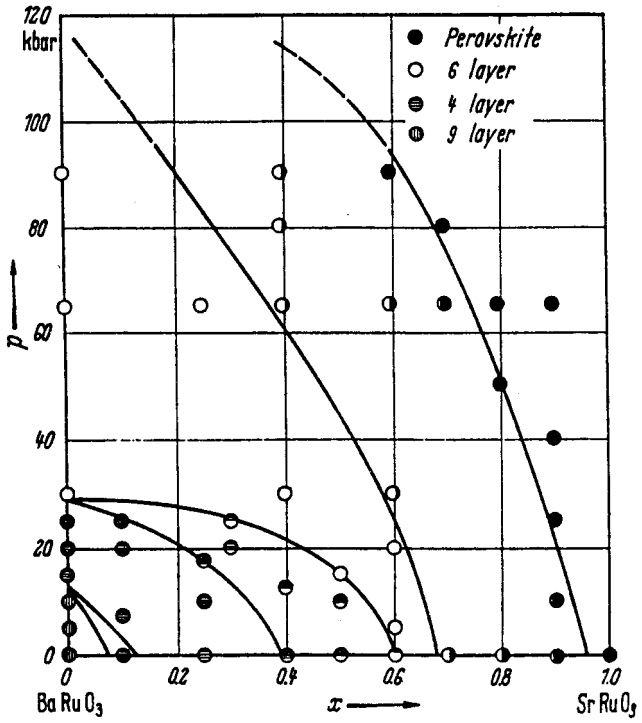

Figure 3. $Ba_{1-x}Sr_xRuO_3$ $P - x$ phase diagram; P = hydrostatic pressure.

be found where aliovalent A cations of different size are present.

The thermal expansion and the compressibility of the A−O bond are normally larger than those of the M−O bond, which is made evident by the relations

$$dt/dT > 0 \quad \text{and} \quad dt/dP < 0 \tag{2}$$

The normal pressure dependence $dt/dP < 0$ has been demonstrated by transforming under pressure hexagonal polytypes to phases with more cubic stacking,[5] as is illustrated in Figure 3. However, at a crossover from localized to itinerant electronic behavior or from a high-spin to a low-spin configuration, a $dt/dP > 0$ is found and is a critical aspect of these crossovers.

B. Virial Theorem. For central-force fields, the virial theorem of mechanics becomes

$$2\langle T\rangle + \langle V\rangle = 0 \tag{3}$$

and a change from localized to itinerant electronic behavior corresponds to a decrease in the mean kinetic energy $\langle T\rangle$ of the electronic system that must be compensated by a decrease in the magnitude of the mean potential energy $|\langle V\rangle|$ of the electrons. The d-like electrons of an MO_3 array that undergo such a change occupy antibonding states, so a shortening of the M−O bond decreases $|\langle V\rangle|$ and is associated with a change from localized to itinerant electronic behavior.[6]

A global change from localized to itinerant electronic behavior would give a discontinuous change in $\langle T\rangle$, and the corresponding discontinuous change in $\langle V\rangle$ would result in a discontinuous change in the equilibrium M−O bond length and hence in a first-order phase change. In this case, the M−O bond energy has a double well at crossover, and the localized-electron phase has an anomalously large compressibility of the M−O bond, which makes $dt/dP > 0$. Moreover, a segregation into an itinerant-electron phase and a localized-electron phase can be expected at a first-order crossover. In the MO_3 array of a perovskite, such a phase segregation can be stabilized at temperatures too low for atomic diffusion by cooperative oxygen-atom displacements that create shorter and longer M−O bond lengths. These cooperative oxygen displacements may be long-range and static or short-range and dynamic (see section IV).

III. Electronic Considerations

A. Valence Electrons and $4f^n$ Configurations. The ionic Madelung energy of an AMO_3 perovskite stabilizes filled bonding bands that are primarily O-2p in character and are separated from antibonding, primarily cationic s and p bands by a large (~6 eV) energy gap. Lanthanide A cations Ln introduce empty 5d states that overlap the antibonding s bands.[7]

The $4f^n$ configurations at the Ln atoms are localized, and the intraatomic electron−electron coulomb energies U separating $4f^n$ and $4f^{n+1}$ configurations are large, $U > 5$ eV. Consequently the Ln atoms can have only a single valence state unless a $4f^n$ configuration falls in the energy gap between the filled O-2p bands and the empty antibonding bands.[8] However, Ce^{4+} is too small to occupy the A site of a perovskite and the Eu^{2+}:$4f^7$ level, which is stable relative to the bottom of the 3d band in $EuTiO_3$, lies above the Fermi energy in the other $EuMO_3$ oxides containing first-long-period transition-metal atoms M.[9] In the perovskite-related oxides to be discussed, only the Pr:$4f^2$ level lies close enough to the Fermi energy ϵ_F of a partially filled band to pose any ambiguity about the valence state of the Ln cation, and this ion only in the presence of the Cu(III)/Cu(II) couple.[10] The examples discussed next all contain Ln^{3+} ions with localized $4f^n$ and $4f^{n+1}$ configurations well removed from the Fermi energy.

B. M-3d Electrons. In the AMO_3 perovskites containing a first-long-period transition-metal atom M, the M-3d electrons may be either localized or itinerant.[11] To understand this phenomenon, we begin with the construction of crystal-field 3d orbitals and then consider the nature of the interactions between localized crystal-field configurations on neighboring M cations and how the crystal-field approximation breaks down.

1. Crystal-Field Considerations. The five 3d orbitals of a free atom are degenerate; but with more than one electron or hole in the 3d manifold, the spin degeneracy is removed by the ferromagnetic direct-exchange interactions between electron spins in orthogonal atomic orbitals. The energy splitting between localized spin states will be designated Δ_{ex}.

The atomic orbitals f_m with azimuthal orbital angular momentum operator L_z, where $L_z f_m = -i\hbar(\partial f_m/\partial\phi) = \pm m\hbar f_m$, have the angular dependencies

$$f_0 \sim (3\cos^2\theta - 1) \sim [(z^2 - x^2) + (z^2 - y^2)]/r^2$$

$$f_{\pm1} \sim \sin 2\theta \exp(\pm i\phi) \sim (yz \pm izx)/r^2$$

$$f_{\pm2} \sim \sin^2\theta \exp(\pm i2\phi) \sim [(x^2 - y^2) \pm ixy]/r^2 \tag{4}$$

In an octahedral site, the xy and $(yz \pm izx)$ orbitals only overlap the neighboring O-$2p_\pi$ orbitals, whereas the $[(z^2$

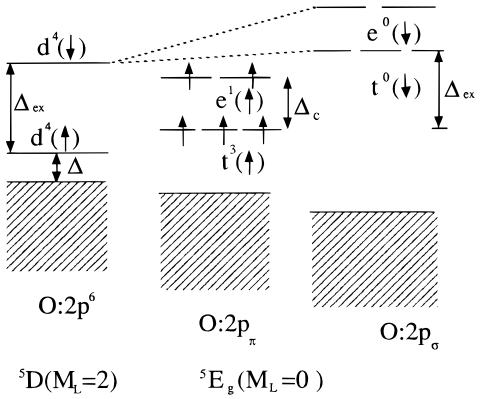

Figure 4. Octahedral-site energies of empty d states of unoccupied Mn^{3+}/Mn^{2+} redox couple relative to the valence-band edge. *Note*: Mn^{3+}:t^3e^1 configuration has 2-fold e-orbital degeneracy; Mn^{2+}:t^3e^2 would be high-spin ($\Delta_{ex} > \Delta_c$) and Mn^{4+}: t^3e^0 would have $t^3(\uparrow)$ and $e^0(\uparrow)$ manifolds lowered by U_π and U_σ, respectively, with $U_\pi > U_\sigma$.

$- x^2) + (z^2 - y^2)]$ and $(x^2 - y^2)$ orbitals only overlap the O-2s, $2p_\sigma$ orbitals. The resonance integrals $b^{ca} \equiv (f_m, H'\phi_O) \approx \epsilon_{mO}(f_m, \phi_O)$ describing the energy of charge transfer to the empty M-3d orbitals from the same-symmetry sum of near-neighbor oxygen orbitals ϕ_O contain both an overlap integral (f_m, ϕ_O) and a one-electron energy (ϵ_{mO}) that are larger for σ-bonding than for π-bonding. Therefore, the antibonding states of a σ-bond are raised higher in energy than those of a π-bond and, as a consequence, the cubic symmetry of the octahedral site raises the 2-fold-degenerate pair of σ-bonding e orbitals, the $[(z^2 - x^2) + (z^2 - y^2)]$ and $(x^2 - y^2)$ orbitals, above the 3-fold-degenerate set of π-bonding t orbitals xy, $(yz \pm izx)$ by an energy Δ_c and quenches the orbital angular momentum associated with $m = \pm 2$ (see Figure 4).

If the empty 3d orbitals of a degenerate manifold lie an energy ΔE_p above the O-2p orbitals and ΔE_s above the O-2s orbitals, the antibonding d-like states may be described in second-order perturbation theory to give the crystal-field wave functions

$$\psi_t = N_\pi(f_t - \lambda_\pi\phi_\pi) \qquad m = 0, \pm 1$$

$$\psi_e = N_\sigma(f_e - \lambda_\sigma\phi_\sigma - \lambda_s\phi_s) \qquad m = 0, 0 \qquad (5)$$

provided the covalent-mixing parameters are $\lambda_\pi \equiv b_\pi^{ca}/\Delta E_p \ll 1$ and $\lambda_\sigma \equiv b_\sigma^{ca}/\Delta E_p \ll 1$. A larger ΔE_s keeps $\lambda_s \ll 1$, where eq 5 is applicable. If ΔE_p becomes too small or becomes negative, the perturbation expansion breaks down and an isolated MO_6 complex must be described by molecular-orbital (MO) theory. According to the second-order perturbation theory, the antibonding states are raised by the M−O interactions an energy

$$\Delta\epsilon = |b^{ca}|^2/\Delta E_i \qquad (6)$$

and the cubic-field splitting is

$$\Delta_c = \Delta\epsilon_\sigma - \Delta\epsilon_\pi = \Delta_M + (\lambda_\sigma^2 - \lambda_\pi^2)\Delta E_p + \lambda_\sigma^2\Delta E_s \qquad (7)$$

where Δ_M is a purely electrostatic energy that is small and of uncertain sign due to the penetration of the O^{2-} ion electron cloud by the crystal-field wave functions. Omitted from eqs 5 and 7 is the interaction of the ψ_t orbitals with the empty A-cation wave functions, which lowers the magnitude of an effective λ_π and increases Δ_c.

The cubic-field splitting Δ_c is the same order of magnitude as the intraatomic exchange energy Δ_{ex}, and the $d^4 - d^7$ configurations may be either high-spin t^3e^1, t^3e^2, t^4e^2, and t^5e^2, where $\Delta_{ex} > \Delta_c$, or low-spin t^4e^0, t^5e^0, t^6e^0, and t^6e^1, where $\Delta_c > \Delta_{ex}$. The covalent mixing of O-2p wave functions into ψ_t and ψ_e lowers the intra-atomic electron−electron coulomb energies, which makes $U_\sigma < U_\pi$; it also lowers the intraatomic exchange splitting Δ_{ex} and increases Δ_c. Therefore, stronger covalent mixing stabilizes low-spin relative to high-spin configurations. Moreover, the effective energy U_{eff} required to add an electron to a d^n manifold to make it d^{n+1} must take into account Δ_c as well as Δ_{ex}:

$$U_{\pi eff} = U_\pi \qquad \text{for } n = 1 \text{ or } 2;\ n = 4 \text{ or } 5 \text{ with } \Delta_c > \Delta_{ex};\ n = 6 \text{ or } 7 \text{ with } \Delta_{ex} > \Delta_c$$

$$= U_\pi + \Delta_{ex} \qquad \text{for } n = 3 \text{ with } \Delta_c > \Delta_{ex};\ n = 5 \text{ with } \Delta_{ex} > \Delta_c$$

$$U_{\sigma eff} = U_\sigma \qquad \text{for } n = 4 \text{ with } \Delta_{ex} > \Delta_c;\ \text{for } n = 7 \text{ or } 9 \text{ with } \Delta_c > \Delta_{ex}$$

$$= U_\sigma + \Delta_c \qquad \text{for } n = 3 \text{ with } \Delta_{ex} > \Delta_c;\ \text{for } n = 6 \text{ with } \Delta_c > \Delta_{ex}$$

$$= U_\sigma + \Delta_{ex} \qquad \text{for } n = 8 \qquad (8)$$

2. Interatomic Interactions. In the perovskite structure, the separation between next-near-neighbor M atoms is too large for significant M−M ψ_t-orbital interactions; the dominant interactions between d-like orbitals centered at M atoms are the $(180° - \phi)$ M−O−M interactions. The spin-independent resonance integrals for these interactions are

$$b_\pi^{cac} \equiv (\psi_{ti}, H'\psi_{tj}) \approx \epsilon_\pi\lambda_\pi^2$$

$$b_\sigma^{cac} \equiv (\psi_{ei}, H'\psi_{ej}) \approx \epsilon_\sigma\lambda_\sigma^2 \cos\phi \qquad (9)$$

where λ_π varies with the acidity of the A cation as well as with ϕ. In the absence of a localized spin on the M atoms, the tight-binding bandwidths for these interactions are

$$W_\pi \approx 2zb_\pi^{cac} \qquad \text{and} \qquad W_\sigma \approx 2zb_\sigma^{cac} \qquad (10)$$

where the number of like nearest neighbors is $z = 6$ for an MO_3 array. Because $\lambda_\sigma > \lambda_\pi$ and ϕ is small, it follows that

$$W_\sigma > W_\pi \qquad (11)$$

A $W_\pi < U_{eff}$ relationship can leave a t^n manifold localized whereas a $W_\sigma > U_{\sigma eff}$ relationship transforms localized e orbitals into an antibonding σ^* band of itinerant-electron states. It is thus apparent that a high-spin $3d^4$ configuration, which has $U_{\pi eff} = U_\pi + \Delta_c > U_{\sigma eff} = U_\sigma$, may satisfy the condition $W_\pi < U_{\pi eff}$ and $W_\sigma > U_{\sigma eff}$, in

which case a localized t^3 configuration coexists with a partially occupied, narrow σ^* band of e-orbital parentage.[12]

Where $\Delta E_p \approx 0$, the perturbation expansion leading to eq 5 is not applicable. In this case, the covalent mixing of M-3d and O-2p states is so extensive that band theory must be used. Nevertheless, covalent mixing gives the antibonding orbitals d-like symmetry and raises them to the top of the O-2p bands. What changes at the crossover $\Delta E_p \approx 0$ is the spectral weight in the antibonding bands from primarily M-3d to primarily O-2p character. Where this happens in a single-valent semiconductive oxide, the energy gap from the top of the filled bands to the lowest unoccupied redox energy has been referred to as a charge-transfer gap Δ as opposed to an intraatomic U_{eff}.[13] However, where the spectroscopist identifies a Δ as against a U_{eff}, further oxidation of a perovskite MO_3 array does not normally introduce holes into bonding or nonbonding O-2p bands, but into a strongly hybridized antibonding band of d-like symmetry. However, a $\Delta E_p \approx 0$ can manifest itself in the formation of molecular orbitals in metal−oxygen clusters or by the formation of itinerant M-3d electrons in antibonding π^* or σ^* bands

IV. Oxygen Displacements

A. Single-Valent MO_3 Arrays. In a single-valent MO_3 array, a variety of long-range cooperative oxygen displacements away from one M-atom near neighbor toward the other have been found. These displacements are superimposed on the cooperative MO_6 rotations associated with a $t < 1$. They require a negative curvature of the d-electron potential-energy curve $\phi(R)$ at the equilibrium bond length R_{eq} for the total potential-energy curve $\Phi(R)$. In this case, $\Delta\epsilon_d \approx (1/2)(\partial^2\phi/\partial R^2)\delta^2 = -A\delta^2$ (where δ is the oxygen displacement) gives an energy gain for the d-like electrons at a cost in elastic energy $\Delta\epsilon_d = B\delta^2 > 0$, and the total energy gained is[14]

$$\Delta\epsilon = -(A - B)\delta^2 \qquad (12)$$

An oxygen-atom displacement can only be stabilized where $A = -(1/2)(\partial^2\phi/\partial R^2)_{Req} > B$. This condition requires, in addition to an $A > 0$, a relatively small B, and hence a large compressibility of the M−O bond at R_{eq}, as occurs where the M−O bond has a double-well potential energy.[6]

Shortening an M−O bond increases the M:3d−O:2p covalent mixing and raises the energies of the antibonding d-like states; lengthening an M−O bond lowers the energies of these states. Where the 3d orbitals of the M cations are empty, as in $BaTiO_3$, no energy is gained by raising some d orbitals and lowering others, so the cooperative oxygen displacements create alternating long and short bonds ···M−O···M−O··· on opposite sides of every M cation, thereby stabilizing the occupied O-2p bonding states at the expense of the empty, antibonding d states. The resulting displacement of each M cation from the center of symmetry of its site results in a ferroelectric or antiferroelectric phase. Such displacements are possible with d^0 or d^1 configurations. However, where the cation has more than one d electron, the cooperative oxygen displacements leave the M cations in the center of symmetry of their site; these displacements either order the electrons among initially degenerate, localized orbitals within an atom or transfer electrons from M atoms in a molecular-orbital cluster to a localized-electron configuration on a neighboring M atom. Three such situations can be distinguished: disproportionation, ordering of high-spin and low-spin configurations, and J−T distortions.

Disproportionation. Cooperative oxygen displacements that shorten all the M−O bonds at every other transition-metal atom M_I and lengthen all the M−O bonds on the neighboring M_{II} atoms can occur in an MO_3 array. Stronger covalent bonding within M_IO_6 complexes and more ionic bonding to M_{II} cations raises the antibonding d-like states of a complex relative to those at the M_{II} cations by an energy ΔE. A $\Delta E > U_{eff}$ condition would result in an electron transfer from the M_IO_6 complex to the M_{II} cations. Such a disproportionation reaction creates a CDW in the crystal, and the physics literature refers to this phenomenon as a "negative-U" CDW because of a $(U_{eff} - \Delta E) < 0$ relationship. Such a CDW changes the periodicity of the electronic potential so as to open an energy gap at the Fermi energy.

Disproportionation is found in the perovskite $CaFeO_3$, which contains high-spin Fe^{4+}:$3d^4$ ions. A $W_\pi < U_\pi + \Delta_c$ condition leaves the t^3 configuration localized, whereas a $W_\sigma > U_\sigma$ condition transforms the crystal-field e orbital into itinerant-electron orbitals of a narrow σ^* band. Mössbauer data[15a] have revealed a progressive splitting of the Fe^{4+} ion spectrum with decreasing temperature below 290 K toward equal populations of $Fe(V)O_6$ complexes and octahedral-site Fe^{3+} ions. The associated oxygen displacements have been confirmed.[15b] In $CaFeO_3$, the σ^* band is narrow enough to satisfy eq 12, whereas in isoelectronic $SrFeO_3$, which has a larger M−O−M bond angle $(180° - \phi)$, the high-spin, metallic configuration $t^3\sigma^{*1}$ does not disproportionate to lowest temperatures.

Jahn−Teller Distortions. The single-valent perovskite $LaMnO_3$ contains an MO_3 array that is isoelectronic with $CaFeO_3$ and $SrFeO_3$, but a $W_\sigma < U_\sigma$ relationship retains a localized t^3e^1 configuration at the high-spin Mn^{3+} ions. In this case, more energy is gained by a cooperative deformation of the octahedral sites from cubic to orthorhombic symmetry that lifts the e-orbital degeneracy; the intraatomic ordering of electrons among localized orbitals does not require an e-orbital splitting $\Delta E > U_\sigma$; it occurs among localized orbitals where U_σ is large. Neutron diffraction data[16] have confirmed the predicted[17] intraatomic orbital ordering by cooperative oxygen displacements within orthorhombic (001) planes that create long O···Mn···O bonds alternating with short O−Mn−O bonds within an $a-b$ plane.

Ordering of High-Spin and Low-Spin Configurations. An intraatomic transition from a low-spin to a high-spin state represents an intraatomic reordering of electrons among d-like orbitals that requires a change in R_{eq} without requiring a change in site symmetry. A greater entropy ΔS is associated with a high-spin state, and the thermal energy $T\Delta S$ can drive a low-spin-to-high-spin transition with increasing temperature. The transfer of antibonding electrons from π-bond to σ-bond orbitals increases R_{eq} at the high-spin cations M_{HS}. In an MO_3 array, the elastic energy associated with a

larger R_{eq} at M_{HS} cations can be minimized by retaining low-spin M_{LS} cations as near neighbors, which involves oxygen displacements $M_{HS}\cdots O-M_{LS}$. A short-range ordering of M_{HS} and M_{LS} cations on alternate M sites of an MO_3 array may be anticipated where the M_{HS}:M_{LS} ratio approaches 50:50. Such ordering would inhibit M−O−M interactions from forming itinerant σ^*-band states until the population of the high-spin ions exceeds 50:50. A greater high-spin population would introduce a compressive stress within high-spin clusters that can be relieved, according to the virial theorem, by a delocalization of the σ-bonding electrons first within isolated clusters and only at higher high-spin concentrations over the entire crystal.

This situation is illustrated by the perovskite $LaCoO_3$, which contains only low-spin Co(III):$t^6\sigma^{*0}$ configurations at lowest temperatures.[18a] However, localized intermediate-spin configurations t^5e^1 are excited rather than high-spin Co^{3+}:t^4e^2.[18b] The population of localized-electron configurations increases progressively with increasing temperature, with a larger R_{eq} at a trivalent cobalt stabilizing localized e^1 configurations. A 50:50 intermediate-spin:low-spin population is approached by room temperature, and above room temperature there is a smooth transition from a semiconductive to a metallic state. The low-spin-to-intermediate-spin transition can be followed by magnetic susceptibility, but the fluctuations between high-spin and low-spin neighbors become fast relative to 10^{-8} s already below room temperature, which has prevented Mössbauer spectra from demonstrating a plateau in the increase in localized intermediate-spin population with temperature at the 50:50 distribution.[19] Such fluctuations cannot be detected by a diffraction experiment. An anomalously large thermal expansion coefficient extending to highest temperatures indicates that the population of σ^*-band electrons continues to increase with temperature until after the metallic state is realized.[20]

B. Mixed-Valent MO_3 Arrays. In a mixed-valent MO_3 array, cooperative oxygen displacements "dress" localized-electron charge carriers. These carriers move diffusively, carrying the local deformations with them. These dielectric polarons are to be distinguished from magnetic polarons. Magnetic polarons are itinerant-electron charge carriers that become confined to regions of short-range ferromagnetic order above a ferromagnetic Curie temperature; they carry a multi-atom volume of ferromagnetic order through a paramagnetic matrix. A nonadiabatic dielectric polaron is normally confined to a single cation site by the shortening or lengthening of all the M−O bonds at that site; shortening confines a mobile hole and lengthening a mobile electron.

At a first-order crossover from localized to itinerant electronic behavior, cooperative oxygen-atom displacements may segregate hole-rich from electron-rich domains. In this case, hole-rich clusters contain molecular d-like orbitals within an electron-rich matrix of localized electrons or electron-rich clusters of localized electrons are segregated from a hole-rich matrix containing itinerant electrons. If these clusters are mobile, they represent nonadiabatic polarons containing more than one cation site.

Table 1. Electronic $3d^n$ Configurations at M Cations of AMO_3 Perovskites with A = La, Y, Sr, and Ca[a]

perovskite	configuration	remarks	ref[b]
$LaTiO_3$	$\pi^{*1}\sigma^{*0}$	AF* (138 K), I, O	1
$YTiO_3$	$\pi^{*1}\sigma^{*0}$	F (30 K), I, O	1
$SrTiO_3$	$\pi^{*0}\sigma^{*0}$	dielectric, I, T−C (110 K)	2
$CaTiO_3$	$\pi^{*0}\sigma^{*0}$	dielectric, I, O	2
$LaVO_3$	$t^2\sigma^{*0}$	AF* (142 K), I, O′−O (137 K)	3
YVO_3	$t^2\sigma^{*0}$	AF* (116 K), I, O′−O (77 K)	4
$SrVO_3$	$\pi^{*1}\sigma^{*0}$	PP, M, C	5
$CaVO_3$	$\pi^{*1}\sigma^{*0}$	PP, M, O	5
$LaCrO_3$	$t^3\sigma^{*0}$	AF* (290 K), I, O	2
$YCrO_3$	$t^3\sigma^{*0}$	AF* (141 K), I, O	2
$SrCrO_3$	$\pi^{*2}\sigma^{*0}$	PP, M, C	2
$CaCrO_3$	$\pi^{*2}\sigma^{*0}$	AF* (90 K), I, O	2
$LaMnO_3$	t^3e^1	AF* (100 K), I, O′−O (875 K)	2
$YMnO_3$	not perovskite		
$SrMnO_3$	$t^3\sigma^{*0}$	hexagonal polytype	
$CaMnO_3$	$t^3\sigma^{*0}$	AF* (142 K), I, O	2
$LaFeO_3$	t^3e^2	AF* (750 K), I, O	2
$YFeO_3$	t^3e^2	AF* (645 K), I, O	2
SrFe	$t^3\sigma^{*1}$	F-helix (130 K), M	6
$CaFeO_3$	$t^3\sigma^{*1}$	AF (115 K), dis (290 K), O	6
$LaCoO_3$	$(1-x)t^6\sigma^{*0} + xt^4e^2 \rightarrow t^{5-\delta}\sigma^{*1+\delta}$	x increases with T smooth I−M, T > 300 K, R	7
$YCoO_3$	$t^6\sigma^{*0}$	diamagnetic, I, O	8
$LaNiO_3$	$t^6\sigma^{*1}$	PP, M, R	9
$YNiO_3$	t^6e^1	AF (140 K), I, O	1
$LaCuO_3$	$t^6\sigma^{*2}$	PP, M, R	9

[a] F = ferromagnet; AF* = canted-spin antiferromagnet; PP = Pauli paramagnet; dis = disproportionation; I = insulator; M = metal; C = cubic; R = rhombohedral; O′ = orthorhombic $c/a < \sqrt{2}$; O = orthorhombic $c/a > \sqrt{2}$; T = tetragonal; critical temperatures in parentheses. [b] References: (1) Arima, T.; Tokura, Y. *J. Phys. Soc. Japan* **1995**, *64*, 2488; (2) Goodenough, J. B.; Longo, J. M. *Landolt-Börnstein Tabellen III/4a*; Springer-Verlag: Berlin, 1970; p 126. (3) Nguyen, H. C.; Goodenough, J. B. *Phys. Rev. B* **1995**, *52*, 324. (4) Ren, Y., et al. *Nature*, in press. (5) Morikawa, K., et al. *Phys. Rev. B* **1995**, *52*, 13711. (6) Gleitzer, C.; Goodenough, J. B. *Struct. Bonding* **1985**, *61*, 1. (7) Señarís-Rodríguez, M. A.; Goodenough, J. B. *J. Solid State Chem.* **1995**, *116*, 224. (8) Kappatsch, A.; Quezel-Ambrunaz, S.; Sivardière, J. *J. Phys. (Paris)* **1970**, *31*, 369. (9) Goodenough, J. B., et al. *Mater. Res. Bull.* **1973**, *8*, 647.

Confinement of a hole-rich cluster to a single MO_6 complex represents a limiting case of phase segregation that can be difficult to distinguish from a localized-electron small polaron. More interesting are cases where cooperative J−T or pseudo-J−T oxygen displacements lower the dynamic symmetry of the sites within a multicenter mobile polaron, especially where the concentration of polarons is high enough to lead to condensation of the polarons into a polaron liquid. Characterization of the dynamic structure of such a liquid requires a faster experimental probe than conventional diffraction techniques. However, the formation of multicenter polarons and a polaron liquid at a crossover from localized to itinerant electronic behavior can have a distinctive influence on the physical properties. Space restrictions prevent exposition here of the manifestations of electronic heterogeneity by the large negative magnetoresistance of the manganese and cobalt mixed-valent oxides with perovskite structure and by the normal-state properties of the high-temperature copper-oxide superconductors having perovskite intergrowth structures.

V. Representative Single-Valent Perovskites

Table 1 summarizes the localized versus itinerant character of the $3d^n$ configurations of the single-valent AMO_3 perovskites with first-long-period transition-

metal atoms M. Configurations t^n and e^m refer to localized electron configurations in a cubic, octahedral-site crystalline field, and the configurations π^{*n} and σ^{*m} refer to itinerant electrons of t-orbital and e-orbital parentage.

A. Localized 3d^n Configurations. *(1) Spin−Spin Interactions.* The interatomic spin−spin interactions between localized-electron configurations are described by *virtual* charge transfers in superexchange perturbation theory.[11] In this case, the electron-transfer energy integral (resonance integral) is spin-dependent:

$$t_{ij}^{\uparrow\downarrow} = b_{ij} \sin(\theta_{ij}/2) \quad \text{and} \quad t_{ij}^{\uparrow\uparrow} = b_{ij} \cos(\theta_{ij}/2) \quad (13)$$

where the b_{ij} are given by eq 9 and θ_{ij} is the angle between spins on neighboring atoms. The superscripts $\uparrow\downarrow$ and $\uparrow\uparrow$ refer, respectively, to antiparallel and parallel spins on the two neighboring cations. The spin angular momentum is conserved in an electron transfer. Rules for the sign of the superexchange interactions follow:

• Superexchange interactions between half-filled orbitals involve electron transfers to half-filled orbitals, which are constrained by the Pauli Exclusion principle to a $t_{ij}^{\uparrow\downarrow}$ and therefore give a

$$\Delta\epsilon_{ex}^{s} = -|t_{ij}^{\uparrow\downarrow}|^2/U_{eff} = \text{const} + J_{ij}\mathbf{S}_{ij}\cdot\mathbf{S}_{ij} \quad (14)$$

where $J_{ij} = (2b_{ij}^2/4S^2U_{eff})$.

• Superexchange interactions between half-filled and empty orbitals, where the empty orbitals belong to a localized-electron configuration with a spin **S**, are not constrained by the Pauli Exclusion Principle, but Hund's intraatomic exchange field favors, by an energy Δ_{ex}, transfer to a spin state that is parallel to the localized spin of the acceptor cation. In this case $t_{ij}^{\uparrow\uparrow}$ is used in third-order perturbation theory to give

$$\Delta\epsilon_{ex}^{s} = \text{const} - J_{ij}\mathbf{S}_{ij}\cdot\mathbf{S}_{j} \quad (15)$$

where $J_{ij} = 2b_{ij}^2\Delta_{ex}/(4S^2U_{eff}^2)$.

(2) Half-Filled Orbitals. Application of these rules to the localized-electron configurations of Table 1 give antiferromagnetic spin−spin interactions between the t^3 configurations and the e^2 configurations of $LaCrO_3$, $CaMnO_3$, and $LaFeO_3$. Antiparallel alignment of spins on nearest-neighbor cations gives type-G antiferromagnetic order. In the orthorhombic structure, a Dzialoshinskii vector $\mathbf{D}_{ij}$ parallel to the *b*-axis allows an additional antisymmetric exchange term $-\mathbf{D}_{ij}\cdot\mathbf{S}_i \times \mathbf{S}_j$ that cants the spins from $\theta_{ij} = 180°$ to give a weak ferromagnetic component.

(3) Jahn−Teller Ions: Mn^{3+} versus V^{3+}. Of more interest are the localized t^2 configurations at the V^{3+} ions of $LaVO_3$ and YVO_3 or the e^1 configurations at the high-spin Mn^{3+} ions of $LaMnO_3$ because, in each case, the cubic-field symmetry leaves the configuration orbitally degenerate (see Figure 5). As discussed in connection with eq 4, the cubic-field splitting quenches the orbital angular momentum of the 2-fold-degenerate e^1 orbitals, but it leaves $m = 0, \pm1$ for the azimuthal orbital angular momentum quantum number of the orbitally 3-fold-degenerate t^2 configuration. Therefore, removal of the orbital degeneracy of the Mn^{3+}:t^3e^1 configuration by a local J−T deformation of the octahedral site to tetragonal or orthorhombic symmetry is not constrained by spin−orbit coupling, and a cooperative J−T distortion of the lattice may occur in the paramagnetic state. On the other hand, a cooperative J−T distortion that removes the orbital degeneracy of a t^2 configuration is constrained by spin−orbit coupling to occur where the spins are ordered nearly collinearly below a magnetic-ordering temperature unless the distortion has a sign that quenches the residual orbital angular momentum (see Figure 5).[21]

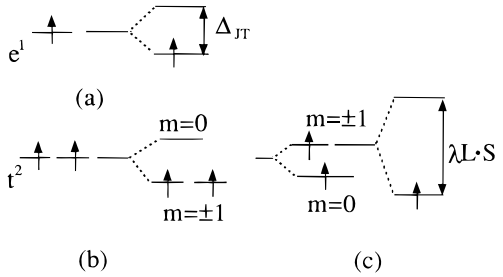

Figure 5. Jahn−Teller removal of orbital degeneracies: (a) e^1, tetragonal ($c/a > 1$) or orthorhombic any *T*, (b) t^2, tetragonal ($c/a > 1$) or rhombohedral ($\alpha > 60°$) $T > T_N$, (c) t^2, tetragonal ($c/a < 1$) or rhombohedral ($\alpha < 60°$) $T < T_N$.

(a) $LaMnO_3$. In $LaMnO_3$, a first-order cooperative J−T distortion of the octahedral sites occurs at a $T_t \approx 875$ K; oxygen-atom displacements within the *a*−*b* planes create long O···Mn···O bonds alternating with short O−M−O bonds such that each Mn atom has two short and two long bonds within an *a*−*b* plane. The J−T distortion is superimposed onto the cooperative MO_6 rotations about a cubic [110] axis responsible for the O-orthorhombic symmetry, so the symmetry remains orthorhombic but with a $c/a < \sqrt{2}$ as opposed to a $c/a > \sqrt{2}$ found where only the rotations occur.[16,17] The low-temperature orthorhombic phase with $c/a < \sqrt{2}$ is designated O′-orthorhombic to indicate the presence of a cooperative J−T deformation. The J−T distortion orders the e^1 electrons into the long O···Mn···O bonds and empties the e orbital of a short O−Mn−O bond, and the *virtual* charge transfer across Mn···O−Mn bonds in the *a*−*b* planes is from a half-filled to an empty e orbital, which gives a ferromagnetic superexchange interaction according to eq 15. The π-bonding t^3 configurations give an antiferromagnetic interaction via eq 14 as in $LaCrO_3$, but weaker π bonding results in a type-A antiferromagnetic order in which ferromagnetic *a*−*b* planes are coupled antiparallel to one another along the *c*-axis.[16,17]

(b) $LaVO_3$ and YVO_3. The orbital angular momentum of the localized V^{3+}:t^2 configuration in $LaVO_3$ and YVO_3 suppresses any cooperative J−T distortion of the VO_6 octahedra in the paramagnetic phase. Spin−orbit coupling also renders the *xy* and (*yz* + i*zx*) orbitals each half-filled, so eq 14 applies to give a type-G antiferromagnetic order below the Néel temperature T_N. Moreover, the Dzialoskinskii vector $\mathbf{D}_{ij}$ is larger where the orbital angular momentum is not quenched, so the two perovskites have a canted-spin type-G antiferromagnetic order with a ferromagnetic component in the *c*−*a* plane. Ordering of the spins below T_N makes possible a cooperative J−T distortion that maximizes the orbital angular momentum; in $LaVO_3$ and YVO_3 such a first-order, cooperative J−T distortion occurs at $T_t = 137$ K $< T_N = 142$ K and $T_t = 77$ K $< T_N = 116$ K,

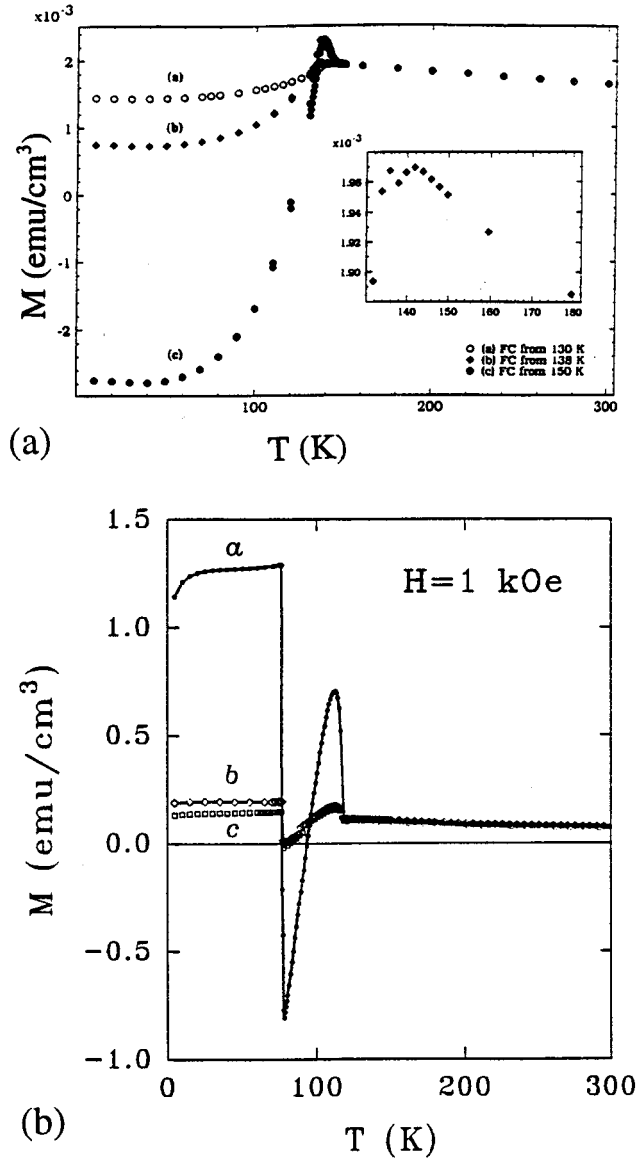

Figure 6. Magnetization curves taken in 1 kOe (a) on heating polycrystalline $LaVO_3$ after cooling to 5 K in 1 kOe from 130 K < T_t, from $T_t \leq$ 138 K < T_N, and from 150 K > T_N, and (b) from ref 27, on cooling a single crystal of YVO_3 with field along the *a*-, *b*-, and *c*-axes, respectively. Inset of (a): Double peak after cooling from 138 K $\approx T_t$ shows character of both field-cooled and zero-field-cooled curves.

respectively.[22,23] Remarkably, the phase transition orients the ferromagnetic component in opposition to the internal magnetic field. In $LaVO_3$, the internal field is in the direction of the applied field $\mathbf{H}_a$ in the interval $T_t < T < T_N$, and cooling through T_t in $\mathbf{H}_a$ induces an anomalously large diamagnetism[24,25] (see Figure 6a) that, as was subsequently demonstrated,[26] is due to an orientation of the ferromagnetic component in opposition to $\mathbf{H}_a$. Antisymmetric exchange constrains the spins to lie in the *c*−*a* plane. In YVO_3, a rotation of the crystallographic easy axis of magnetization within the *c*−*a* plane reverses the sign of the ferromagnetic component along the *a*-axis on cooling in the interval $T_t < T < T_N$; and on cooling through T_t, the sign of the magnetization is reversed back into the direction of $\mathbf{H}_a$, as shown in Figure 6b.[27] This quite spectacular result appears to be due to the first-order character of the J−T transition that enhances the orbital moment at the V^{3+} ions. A discontinuous change in the orbital moment would induce a response in the persistent atomic currents that give rise to the orbital angular momentum; the response would oppose the change in accordance with Lenz's law and reverse the direction of the Dzialoshinskii vector on passing through the transition.

B. Itinerant 3d Electrons. The situation in $SrFeO_3$ and $CaFeO_3$ is to be contrasted with that in $LaMnO_3$, and the behavior of $SrCrO_3$ and $CaCrO_3$ is to be contrasted with that of $LaVO_3$ and YVO_3. Whereas the localized electron configurations have an orbital degeneracy removed by a J−T deformation of the local site symmetry, itinerant electrons occupy one-particle states of the entire crystal; no crystal deformations analogous to the cooperative J−T distortions are found with itinerant electrons. However, the occupied states of an itinerant-electron band may be stabilized relative to unoccupied states by a change of the translational symmetry of the lattice rather than of the point symmetry of a cation site. Changes in the translational symmetry may introduce either a CDW or a spin-density wave (SDW) in the crystal with a propagation vector **q**.

1. $SrFeO_3$ and $CaFeO_3$. From eqs 9 and 10, the σ^* bands of e-orbital parentage have a width

$$W_\sigma \approx 2z\epsilon_\sigma\lambda_\sigma^2 \cos\phi \qquad (16)$$

where ϕ is a measure of the bending of the (180° − ϕ) M−O−M bond angle. Because the t^3 configurations of $SrFeO_3$ and $CaFeO_3$ remain localized with a sin S = 3/2, it is necessary to replace b_σ^{cac} with the spin-dependent resonance integral $t_\sigma^{\uparrow\uparrow} = b_\sigma^{cac}\langle\cos(\theta_{ij}/2)\rangle$, and the bandwidth becomes

$$W_\sigma \approx 2z\epsilon_\sigma\lambda_\sigma^2 \cos\phi\langle\cos(\theta_{ij}/2)\rangle \qquad (17)$$

where cos ϕ decreases with the tolerance factor t and therefore with both decreasing temperature and A cation size.

In $SrFeO_3$, W_σ remains wide enough that no CDW is formed. However, the intraatomic Hund exchange energy Δ_{ex} polarizes the band-electron spins parallel to the localized spin S = 3/2 of the t^3 configurations in the neighborhood of each cation and introduces an indirect (RKKY) interatomic interaction between localized spins that oscillates from ferromagnetic to antiferromagnetic with increasing separation of the interacting localized spins. Ferromagnetic nearest-neighbor and antiferromagnetic next-nearest-neighbor interactions can give rise to a ferromagnetic-helix spin configuration propagating along a cubic [111] axis, and such a configuration with a $|q| = 0.112(2\pi/a_o)$ has been observed by neutron diffraction.[28]

Substitution of a smaller Ca for Sr increases ϕ, which narrows W_σ, and below 290 K the disproportionation reaction

$$2Fe^{4+} = Fe_I^{(4-\delta)+} + Fe_{II}^{(4+\delta)+} \qquad (18)$$

sets in smoothly with δ increasing toward unity with decreasing temperature.[15] This disproportionation reflects the concentration of the itinerant-electron character in molecular orbitals of $Fe_{II}O_6$ and the introduction of a localized-electron character at the Fe_I atoms. This

behavior is but one possible response to the approach to localized-electron behavior as an itinerant-electron bandwidth is narrowed.

2. $SrCrO_3$ and $CaCrO_3$. Substitution of Ca for Sr narrows a π^* bandwidth, as illustrated by the chromates in Table 1. Whereas $SrCrO_3$ remains a Pauli-paramagnetic metal to lowest temperatures, $CaCrO_3$ becomes antiferromagnetic with a $T_N \approx 90$ K. The itinerant character of the antiferromagnetism of $CaCrO_3$ has been demonstrated by a $dT_N/dP < 0$;[29] a $dT_N/dP > 0$ for localized t^2 configurations follows from eq 14 because b_{ij} increases and $U_{\pi\text{eff}} = U_\pi$ decreases with hydrostatic pressure P. The sign of the interatomic spin−spin interactions does not change with the breakdown of the superexchange perturbation theory associated with localized electrons, but the sign of dT_N/dW does change.[30] On the other hand, these experiments tell us little about whether the character of the electrons changes smoothly or abruptly on passing from itinerant to localized character.

3. $Sr_{1-x}Ca_xVO_3$. According to the virial theorem, we may anticipate an abrupt transition from strongly correlated, itinerant quasiparticles to localized electrons. In a single-valent system, such an abrupt transition could manifest itself as a global dilatation of the lattice on passing from itinerant to localized electronic character. Such a transition is observed in the quenched-in $B8_1$ phase of NiS.[31] Alternatively, it could manifest itself in the perovskite structure as localized-electron fluctuations in an itinerant-electron matrix, with cooperative oxygen displacements stabilizing localized-electron domains of larger mean M−O bond length that fluctuate over time. Observation of such dynamic fluctuations would require a fast experimental probe. One such probe is photoemission spectroscopy (PES).

Morikawa et al.[32] have performed an elegant study of $SrVO_3$ and $CaVO_3$ with inverse photoemission and high-resolution PES. $SrVO_3$ and $CaVO_3$ are both Pauli-paramagnetic metals, but W_π is narrowed by the substitution of Ca for Sr just as in the chromates. $CaVO_3$ becomes antiferromagnetic with only small deviations from stoichiometry, which indicates that the transition from itinerant to localized electronic behavior is being approached from the itinerant-electron side. The PES data show the coexistence of two d-electron spectra: one corresponds to incoherent (localized-electron) states at energies well below the Fermi energy ϵ_F and the other to coherent (itinerant-electron) states with a sharply defined Fermi surface (see Figure 7). Moreover, Figure 7 shows a significant transfer of states from the coherent to the incoherent spectrum in $CaVO_3$ compared with $SrVO_3$ as should be expected for narrower π^* bands in $CaVO_3$. These data demonstrate that, in the absence of a static phase segregation into localized-electron configurations and molecular-orbital clusters, as appears to occur in $CaFeO_3$, there can be a dynamic segregation into localized-electron configurations within a matrix containing itinerant electrons without the stabilization of a global, itinerant-electron antiferromagnetic or SDW phase. This behavior is quite different from the Mott−Hubbard picture[33] of a smooth, global opening of an energy gap as the bandwidth of a single-valent system narrows from that of a Pauli-paramagnetic metal to that of a magnetic insulator.

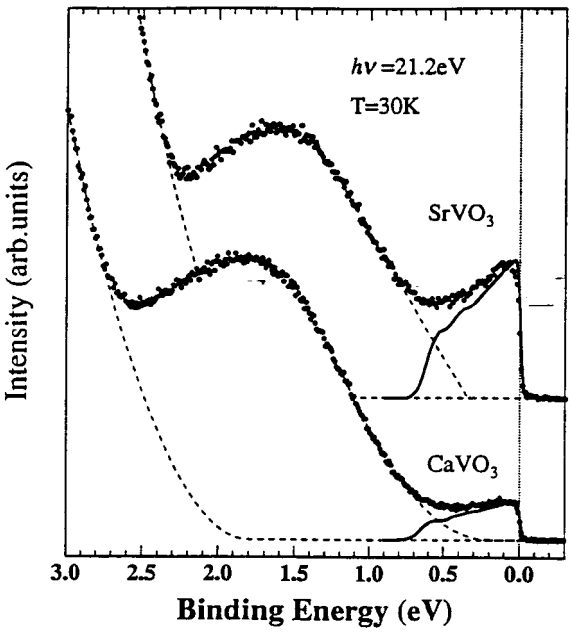

Figure 7. High-resolution photoemission spectra taken at $T \approx 30$ K.[32] Dashed curves are decomposition of the tail of the O-2p valence band and the incoherent part of the V-3d spectrum. Solid curves are densities of states of coherent spectral weight taken from an LDA band-structure calculation narrowed by a factor m_b/m^*.

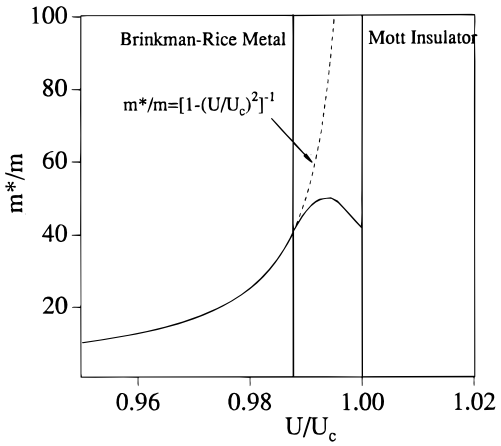

Figure 8. Schematic variation of a normalized effective mass versus the normalized Hubbard energy U for a mass-enhanced metal. Deviation from Brinkman−Rice (dashed) curve occurs where coherent and incoherent states coexist.

Similar measurements and analysis of the $Sr_{1-x}Ca_xVO_3$ system[34] show a continuous transfer of states with increasing x from the coherent to the incoherent spectrum. It is also possible to extract from the PES data a measure of the ratio m^*/m_b, where m^* and m_b are, respectively, the effective and bare mass of the itinerant electrons; the data show a ratio of m^*/m_b that passes through a maximum value with increasing x.

Brinkman and Rice[35] have predicted a ratio

$$m^*_{e-e}/m_b = [1 - (U_{\text{eff}}/U_c)^2]^{-1} \qquad (19)$$

for a strongly correlated, globally homogeneous system of electronic quasiparticles. This ratio is plotted in Figure 8. Also shown is the implication of the PES data; viz., a departure from the Brinkman−Rice prediction

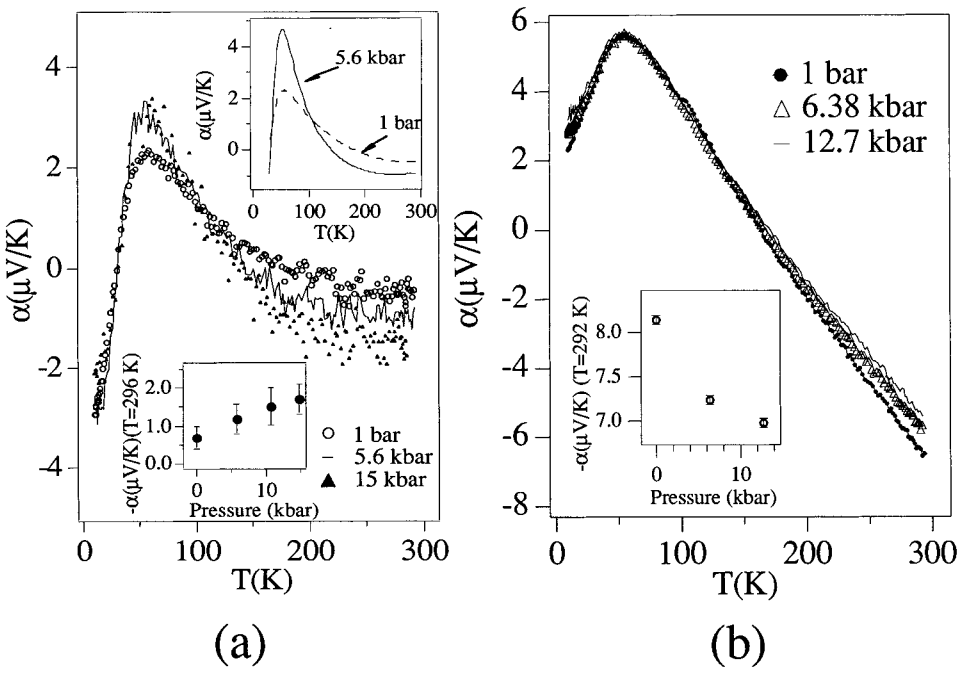

Figure 9. Temperature dependence of the Seebeck coefficient $\alpha(T)$ of (a) $CaVO_3$ and (b) Pt under different hydrostatic pressures P in a self-clamped device. Lower insets: α(room T) versus P. Upper inset of (a): fitted curves corrected for a uniform P over temperature.

where the homogeneous system breaks down into a heterogeneous electronic system and m_{e-e}^*/m_b reaches a maximum within the range $U_c - U_{\pi eff}$, where localized and itinerant electrons coexist. To test whether the maximum in m^*/m_b found in the $Sr_{1-x}Ca_xVO_3$ system is a true reflection of the approach of $U_{\pi eff} = U_\pi$ to U_c, as indicated in Figure 8, or is a consequence of the presence of two different isovalent A cations, we[36] studied the temperature dependence of the thermoelectric power, $\alpha(T)$, of $CaVO_3$ as a function of hydrostatic pressure P. The thermoelectric power of a polycrystalline sample is a transport property that is not affected by the grain boundaries. Hydrostatic pressure increases the bandwidth W_π and reduces U_π/U_c, which is why m^*/m_b would decrease with applied pressure in a conventional homogeneous electronic system. $CaVO_3$ is chemically homogeneous, and the PES data would place U_π close to U_c in Figure 5. If the maximum in m^*/m_b indicated in Figure 8 is representative of a heterogeneous electronic system, reduction of U_π/U_c by pressure in $CaVO_3$ should increase m^*/m_b, contrary to the prediction for a homogeneous system. Figure 9 shows the results of our pressure experiments on $CaVO_3$.

Interpretation of Figure 9 begins with a general expression for the thermoelectric power:

$$\alpha = \alpha_0 + \delta\alpha \tag{19}$$

where $\delta\alpha$ is a low-temperature enhancement or phonon-drag component. Above room temperature, $\alpha \approx \alpha_0$ where

$$\alpha_o = -\frac{k}{e}\int \frac{(\epsilon - \epsilon_F)}{kT}\frac{\sigma(\epsilon)}{\sigma}\,d\epsilon \tag{21}$$

in which $\sigma(\epsilon) = f(\epsilon)[1 - f(\epsilon)]N(\epsilon)\,\mu(\epsilon)$ is the product of the Fermi distribution function $f(\epsilon)$, the energy density of one-particle states $N(\epsilon)$, and the particle mobility $\mu(\epsilon)$ at an energy ϵ relative to a band edge. In a metallic conductor, α_o becomes Mott's expression

$$\alpha_o \approx -\frac{\pi^2 k^2 T}{3e\epsilon_F}\left\{\frac{\partial \ln \sigma(\epsilon)}{\partial \ln \epsilon}\right\}_{\epsilon=\epsilon_F} \tag{22}$$

A band-structure calculation[37] indicates the Fermi surface is not strongly perturbed by its interaction with the Brillouin-zone boundary, so the factor $\{\partial \ln \sigma(\epsilon)/\partial \ln \epsilon\}_{\epsilon=\epsilon_F}$ should be insensitive to volume changes. In this case, the pressure sensitivity of α_o for an electron gas varies as $1/\epsilon_F \sim V^{2/3}$. Electron−phonon interactions of coupling strength λ introduce into α a factor $(1 + \lambda)$ that is also pressure dependent.[38] In a homogeneous electronic system, this factor gives rise to an effective mass m^*_{e-ph} that is calculated by a similar renormalization procedure as that used by Brinkman and Rice[35] to obtain m^*_{e-e}/m_b due to electron−electron interactions. Therefore we assumed that m^*_{e-e}/m_b adds another pressure-dependent factor to α, and we considered the pressure dependence of

$$\alpha \approx (m^*_{e-e}/m_b)(1 + \lambda)\alpha_o \tag{23}$$

Broadening of a bandwidth by the application of hydrostatic pressure reduces the curvature of $\epsilon(k)$ so as to reduce $(1 + \lambda)$ as well as the volume V. Moreover, placement of U_π/U_c to the left of the maximum in m^*_{e-e}/m_b in Figure 8 would also give rise to an m^*_{e-e}/m_b that decreases with pressure, so we could predict unambiguously a $\partial|\alpha(300\text{ K})|/\partial P < 0$ for a conventional metal with a homogeneous electronic system, which is what was observed in Figure 9 for α(300 K) of Pt. On the other hand, Figure 9 shows a $\partial|\alpha(300\text{ K})|/\partial P > 0$ for $CaVO_3$, which can only be explained within the framework of the previous discussion if m^*_{e-e}/m_b increases with the bandwidth (i.e., with decreasing U_π/U_c). This finding is consistent with the analysis of the PES data, which

found a maximum in m^*/m_b with increasing x in the system $Sr_{1-x}Ca_xVO_3$. We conclude that the maximum in m^*/m_b is an intrinsic property of a heterogeneous electronic system and is not an artifact of the presence of two A cations of different size.

The other significant feature of Figure 9 is the difference in the effect of hydrostatic pressure on the phonon-drag term $\delta\alpha$ for Pt and $CaVO_3$. At ambient pressure, both Pt and $CaVO_3$ show a phonon-drag enhancement with a $T_{max} \approx 60$ K that is characteristic of a metal with a $T_{max} \approx 0.2\theta_D$, where θ_D is the Debye temperature. This enhancement becomes negligible at room temperature because $\delta\alpha/\alpha_0 \sim T^{-2}$.[39] A modest electron−phonon coupling parameter λ and long-range acoustic phonons are prerequisites for the phonon-drag effect. In the pressure range of our experiments, pressure would produce a negligible change in λ and θ_D, so no appreciable change in either T_{max} or the magnitude of $\delta\alpha$ can be anticipated for a homogeneous electronic system, as is demonstrated for Pt. On the other hand, the magnitude of $\delta\alpha$ in $CaVO_3$ is seen to increase dramatically with pressure, a response that can only, to our knowledge, be understood if pressure increases the correlation length of the phonons. This deduction is also consistent with the PES evidence for a heterogeneous electronic system in which the concentration of localized-electron fluctuations decreases with increasing bandwidth. Localized-electron fluctuations would enhance a Pauli-paramagnetic susceptibility; they need not introduce a Curie−Weiss type of temperature dependence. We therefore conclude that suppression of $\delta\alpha$ in a chemically homogeneous metallic system is a signature of an electronically heterogeneous system and that the diagram of Figure 8 is qualitatively correct.

4. The $La_{1-x}Nd_xCuO_3$ System. Metallic $LaCuO_3$, which is prepared under high oxygen pressure,[40] has a narrow, half-filled σ^* band; it exhibits an enhanced Pauli-paramagnetic susceptibility that has been interpreted[41] to be due to a Brinkman−Rice enhancement of m^*_{e-e} associated with a $U_{eff} = U_\sigma$ approaching U_c. Substitution of the smaller Nd^{3+} ion for La^{3+} decreases the $(180° - \phi)$ Cu−O−Cu bond angle, which from eq 16 narrows W_σ without changing the oxidation state of the CuO_3 array. In an attempt to narrow W_σ to the limit $U_\sigma = U_c$, $La_{1-x}Nd_xCuO_3$ samples were prepared under high oxygen pressure; but single-phase samples could only be obtained over the range $0 \le x \le 0.5$.[42] We were not able to obtain a high-pressure phase that converted at ambient pressure to a localized-electron phase. Nevertheless, the enhancement of the Pauli-paramagnetic susceptibility increased with x, as anticipated, and the samples remained metallic for all x.

Figure 10 shows plots of $\alpha(T)$ under different hydrostatic pressures P for samples $x = 0$, 0.25, and 0.5 of the system $La_{1-x}Nd_xCuO_3$ for comparison with the data of Figure 9 for $CaVO_3$. Of particular interest is the value of α(300 K) and the change with x and P in the magnitude of the phonon-drag component $\delta\alpha$, which is negative in this system. The magnitude of α(300 K) for all x is as small as that of elemental copper, which distinguishes these copper oxides from other metallic oxides with partially filled σ^* bands. From the Mott expression (eq 22), a small α_o(300 K) indicates either little curvature of the $\epsilon(\mathbf{k})$ dispersion curves at ϵ_F or a fortuitous cancellation of positive and negative contributions coming from different parts of the Fermi surface. A significant, positive α(300 K) would be predicted from the calculated[43] band structure for $LaCuO_3$, which casts doubt on the homogeneous quasiparticle assumption on which the band-structure calculation was based. Moreover, the Nd-doped samples exhibit a small increase in α_o(300 K) with pressure and a decrease with increasing Nd concentration x; both of these observations indicate m^*_{e-e}/m_b increases with

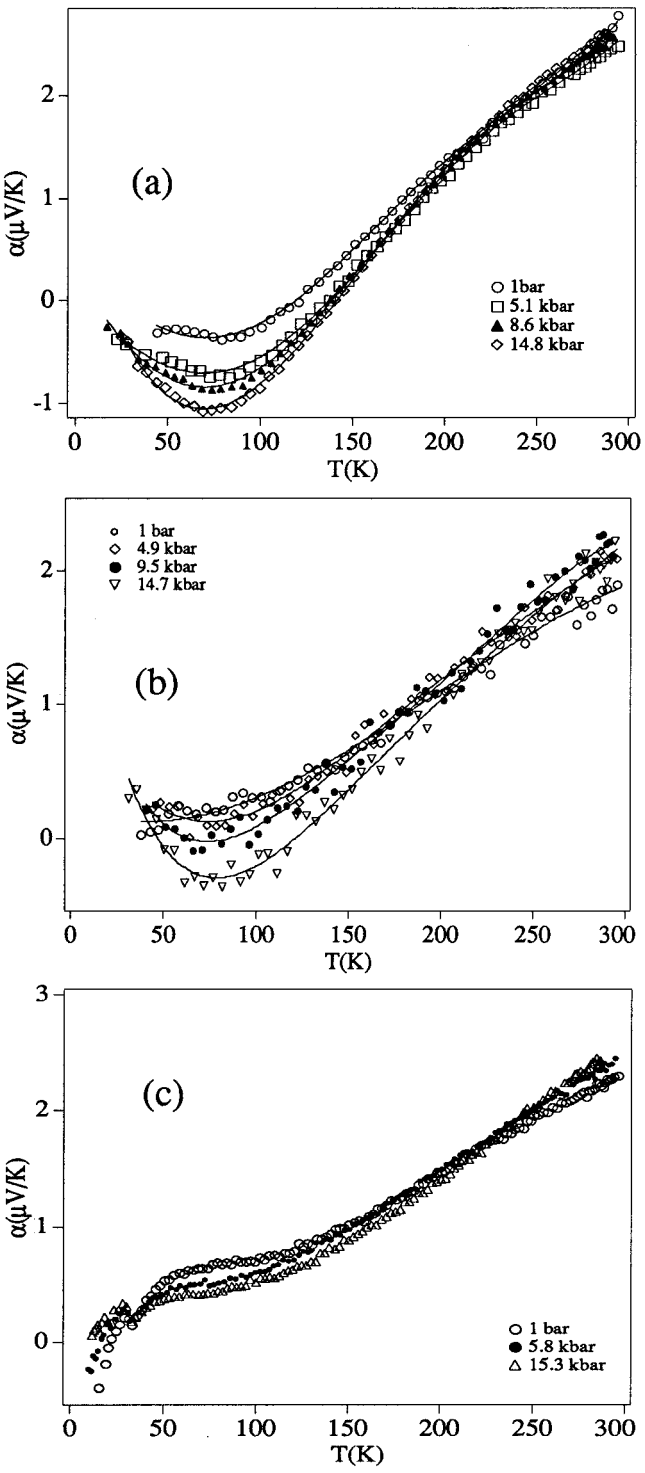

Figure 10. Temperature dependence of the thermoelectric power $\alpha(T)$ of $La_{1-x}Nd_xCuO_3$ under different pressures for (a) $x = 0$, (b) $x = 0.25$, and (c) $x = 0.5$

increasing bandwidth W_σ as in the case of $CaVO_3$, which would locate the $x = 0.5$ sample near the $U_{\sigma\text{eff}} = U_c$ boundary in Figure 8 and the $x = 0$ sample near the bandwidth with a maximum m^*_{e-e}. Moreover, the phonon-drag component $\delta\alpha(T)$ is gradually suppressed as x increases at atmospheric pressure; it nearly disappears in the $x = 0.5$ sample. However, the magnitude of $\delta\alpha(T)$ increases with P. Because high pressure would have no influence on an impurity-scattering mechanism, we are forced to conclude, as for $CaVO_3$, that strong heterogeneous electron−lattice interactions progressively reduce the phonon coherence length with decreasing width of the conduction band. Thus, Figure 8 appears to apply to the narrow-band system $La_{1-x}Nd_xCuO_3$ as well as to $Sr_{1-x}Ca_xVO_3$.

C. Crossover without Coexistence of Localized Spins. The $LnTiO_3$ and $LnNiO_3$ families in which Ln is a trivalent lanthanide or yttrium provide examples of single-valent perovskites at the crossover from itinerant to localized electronic behavior. The TiO_3 array contains Ti^{3+}:$\pi^{*1}\sigma^{*0}$ configurations with quasi-degenerate π^* bands of t-orbital parentage that are one-sixth filled, a configuration that is analogous to the VO_3 array of the $Sr_{1-x}Ca_xVO_3$ system. The NiO_3 array contains low-spin Ni(III):$t^6\sigma^{*1}$ configurations with 2-fold-degenerate σ^* bands of e-orbital parentage that, as in the case of $SrFeO_3$ and $CaFeO_3$, are one-quarter filled. However, in the NiO_3 array, the σ^*-band electrons do not coexist with a localized spin on a t^3 configuration, but with a filled t^6 configuration.

(1) $LnTiO_3$ (Ln = Rare-Earth or Yttrium). $LaTiO_3$ is semiconductive with a strongly enhanced Pauli paramagnetism at temperatures $T > T_N \approx 138$ K; below a second-order transition at T_N, it becomes a weakly ferromagnetic semiconductor with a canted-sin type-G antiferromagnetic order and a semiconductive energy gap $E_g \approx 0.2$ eV.[44] PES data of Fujimori et al.[45] show a small fraction of coherent states coexisting with a large fraction of incoherent states. $YTiO_3$, on the other hand, is a ferromagnetic insulator with an energy gap $E_g \approx 1.2$ eV and a Curie−Weiss paramagnetism above $T_c \approx 30$ K.[46] The PES data for this perovskite show only incoherent electronic states are present; but there is no J−T deformation below T_c of the O-orthorhombic structure as occurs in $LaVO_3$ and YVO_3 structure where the t^2 configuration is localized.

In a single-valent, electronically homogeneous MO_3 array, strong electron−electron interactions within narrow, degenerate bands that are less than one-quarter filled have been predicted[47] to give itinerant-electron ferromagnetic order in a semiconductive phase with a band gap $E_g = U - W$ without any localized-electron J−T deformation below T_c. The ferromagnetic order of $YTiO_3$ with an $E_g \approx U_\pi - W_\pi = 1.2$ eV fits this description. In a homogeneous ferromagnetic system, the paramagnetic susceptibility obeys a Curie−Weiss law.

The larger $(180° - \phi)$ Ti−O−Ti bond angle in $LaTiO_3$ and the more ionic character of the La−O bond relative to the Y−O bond broaden the π^* bands of $LaTiO_3$ relative to those of $YTiO_3$. Consequently, the electron−electron interactions are weaker in $LaTiO_3$; nevertheless, they remain strong enough to retain a $U_\pi \geq U_c$. In $CaVO_3$, a $U_\pi < U_c$ relationship leaves the electronic system Pauli paramagnetic, but enhanced, to lowest temperatures; in $LaTiO_3$, an enhanced Pauli paramagnetism is retained above T_N, but a $U_\pi \geq U_c$ relationship induces magnetic order below T_N. The PES data[45] for $LaTiO_3$ demonstrate that the heterogeneous character of the electronic system found in $CaVO_3$ persists in $LaTiO_3$ across the critical bandwidth where $U_\pi = U_c$. Above T_N, the fluctuating moments associated with incoherent states strongly enhance the Pauli-paramagnetic susceptibility of the electronic system without introducing a Curie−Weiss temperature dependence as in $CaVO_3$.[48] However, below T_N stabilization of a SDW locks these moments into a static spin configuration. Stabilization of the SDW opens a gap $E_g = U_\pi - W_\pi$ at the Fermi energy in the coherent-state band to give a small $E_g \approx 0.2$ eV.

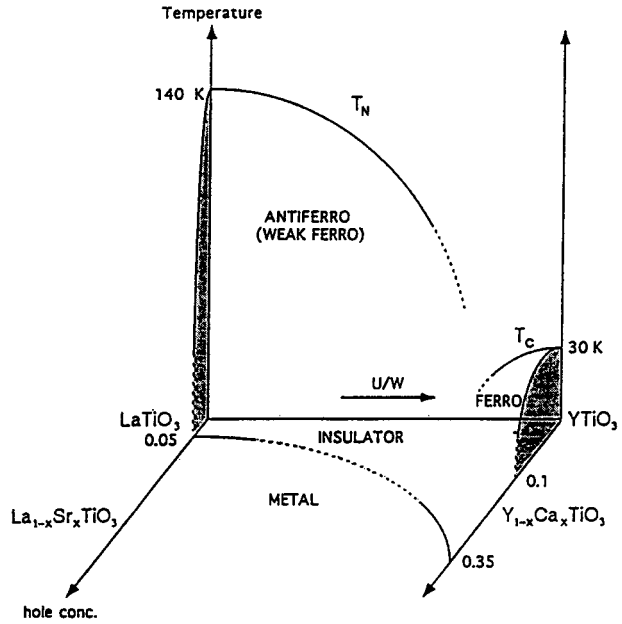

Figure 11. Magnetic phase diagram for $La_{1-x}Y_xTiO_3$.[51]

The evolution of the magnetization with decreasing bandwidth W_π can be obtained by varying the angle ϕ of the $(180° - \phi)$ Ti−O−Ti bond angle. The angle ϕ decreases with the size of the rare-earth ion Ln in the family $LnTiO_3$ and with x in the system $La_{1-x}Y_xTiO_3$. Chemical homogeneity is preserved in the $LnTiO_3$ family, but the magnetic moments of the rare-earth ions change. The evolution of the magnetic properties of the TiO_3 array with changing ϕ is similar for the $LnTiO_3$ family and the $La_{1-x}Y_xTiO_3$ system, which indicates any interaction between the rare-earth magnetic moments and the π^* electrons is weak. The Néel temperature T_N decreases with increasing ϕ from 138 K for $LaTiO_3$ to ~50 K in $SmTiO_3$;[49] europium is present as Eu^{2+} in $EuTiO_3$, and by $GdTiO_3$ the TiO_3 array has become ferromagnetic with a $T_c \approx 34$ K.[50] Figure 11 shows the evolution with x of T_N and T_C in the $La_{1-x}Y_xTiO_3$ system.[51] Raman scattering[52] indicates that T_N decreases with the coherent-electron density at the Fermi energy ϵ_F, which is consistent with a stabilization of the antiferromagnetic phase by the formation of a SDW. Optical spectra[53] show a sharpening of the incoherent-band absorption edge with a decrease in the fraction of coherent states as $(180° - \phi)$ decreases. It follows from these data that the pressure dependence $dT_N/dP > 0$

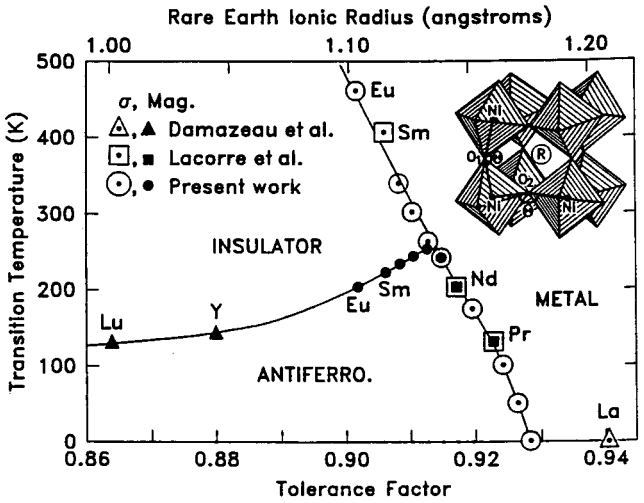

Figure 12. Magnetic and electronic $T - t$ phase diagram for the $LnNiO_3$ family, according to ref 55.

observed[54] for $LaTiO_3$ does not reflect the pressure dependence of the superexchange interaction of eq 14 for localized spins on the Ti^{3+} ions, but a transfer of spectral weight from incoherent to coherent states with increasing W_π, which increases the density of coherent states at ϵ_F.

(2) $LnNiO_3$ (Ln = Rare-Earth or Yttrium). The $LnNiO_3$ family undergoes a transition from an enhanced Pauli paramagnetism in metallic $LaNiO_3$ to a Curie−Weiss paramagnetism with antiferromagnetic order below a T_N in the insulators $LuNiO_3$ and $YNiO_3$. Figure 12 shows the evolution with tolerance factor t of a global first-order insulator−metal transition T_{IM} and the Néel temperature T_N.[55] With the exception of $LaNiO_3$, all the perovskites have the O-orthorhombic structure at room temperature; an orthorhombic−rhombohedral transition occurs at a $T_{OR} > T_{IM}$. On cooling through T_{IM}, the volume expands by 0.2% as a result of a small increase in the average Ni−O bond length of ∼0.004 Å; the Ni−O−Ni bond angles decrease by $\Delta\theta \approx -0.5°$.[56] However, no reduction in the symmetry of the local NiO_6 octahedra could be detected by neutron diffraction, and the crystal symmetry remained O-orthorhombic across T_{IM}. The magnetic transition at $T_N < T_{IM}$ is second-order, but it is first-order in $NdNiO_3$ and $PrNiO_3$, where $T_N = T_{IM}$. Below T_N, the antiferromagnetic order is unusual;[57,58] it can be represented as a SDW propagating along a [111] axis with Ni−O−Ni spin−spin interactions that alternate between ferromagnetic and antiferromagnetic; the nickel moment obtained by neutron diffraction is $\mu_{Ni} \approx 0.9\mu_B$, but it appeared to increase to $1.2\mu_B$ in $EuNiO_3$. An isotope exchange of ^{18}O for ^{16}O had no effect on the structure or on $T_N < T_{IM}$ and the orthorhombic−rhombohedral transition temperature $T_{OR} > T_{IM}$, but it increased T_{IM} significantly:[59] $\Delta T_{IM} = T_{IM}(^{18}O) - T_{IM}(^{16}O) = +10.3, +8.5, +7.6, +3.1$, and $+1.7$ K for $Ln = La_{0.1}Pr_{0.9}$, Pr, Nd, Sm, and Eu, respectively. Moreover, $T_{IM}(^{16}O)$ decreases and ΔT_{IM} increases linearly with $\cos\phi \sim W_\sigma$.

Interpretation of these quite remarkable findings begins with the observation that the Ni(III) ions are in their low-spin configuration $t^6\sigma^{*1}$ and that a Ni(III)/Ni^{2+} redox energy lies close to the O^{2-}:$2p^6$ energy level in an ionic model; an ionic model has a charge-transfer gap $\Delta \approx 0$, which means there is a breakdown of the perturbation expansion of eq 5 for the crystal-field wave function ψ_e. The result is a massive covalent mixing of Ni-e and O-$2p_\sigma$ orbitals in the itinerant-electron σ^*-band states corresponding to an equilibrium reaction

$$\mathrm{Ni(III)}{:}\sigma^{*1} + \mathrm{O}^{2-}{:}\mathrm{p}_\sigma{}^2 = \mathrm{Ni}^{2+}{:}\mathrm{e}^2 + \mathrm{O}^{-}{:}\mathrm{p}_\sigma{}^1 \quad (24)$$

that is not biased strongly to either the left or the right. A natural interpretation[60] of the unusual antiferromagnetic order below T_N in the insulator phase follows from eq 24: The insulator phase represents a CDW electronic segregation into more strongly covalent Ni−O−Ni interactions alternating with more ionic Ni−O−Ni interactions. Below T_N, the more covalently bonded Ni−O−Ni layers couple ferromagnetically via a covalent-exchange interaction in which the parallel-spin electron O-$p_\sigma(\uparrow)$ occupies a molecular orbital of a Ni−O−Ni bond to couple parallel the Ni-e(↑) of the two neighboring Ni atoms via an intrabond direct-exchange interaction between electrons in orthogonal molecular orbitals. The 2-fold e-orbital degeneracy at the Ni(III) atoms makes possible the preferential transfer of O-$p_\sigma(\uparrow)$ electrons into the empty e(↑) orbitals. On the other hand, the ferromagnetic Ni−O−Ni layers are coupled antiferromagnetically by superexchange coupling across the more ionic O^{2-} ions that separate them.

The CDW in the insulator $LnNiO_3$ phases is to be contrasted with the negative-U CDW that develops in $CaFeO_3$. In $CaFeO_3$, covalent bonding is concentrated in an $Fe_{II}O_6$ complex and parallel-spin electrons are transferred to a more ionically bonded $Fe_I^{(4-\delta)+}$ ion (eq 18). Which of these CDWs is the more stable depends on the relative energies of U_σ and Δ for the two systems; it appears that a $U_\sigma < \Delta$ controls the CDW formation in $CaFeO_3$, and a $\Delta < U_\sigma$ in the $LnNiO_3$ family.

It is also to be noted that $LaNiO_3$ is a bad metal and that the first-order transition at T_{IM} in $PrNiO_3$ exhibits a large isotope shift. These observations suggest that the static CDW postulated for the insulator phase becomes dynamic in the "bad-metal" phase with a retention of strong electron interactions with optical phonons. A transition from a static to a dynamic CDW would, according to the virial theorem, be compatible with the first-order transition at T_{IM} and a larger mean Ni−O bond length in the insulator phase. It is also consistent with the large isotope shift of T_{IM}, a heavier oxygen mass stabilizing the static CDW to a higher T_{IM}. Moreover, a narrower W_σ would increase T_{IM}, but reduce the kinetic energy of the mobile CDWs in the "metallic" phase so as to reduce ΔT_{IM} and the volume change ΔV at T_{IM}. Pressure has a dramatic effect on T_{IM}; a common rate of decrease $dT_{IM}/dP = -4.2$ K/kbar has been reported,[61] a broader W_σ decreasing T_{IM}. In this family, a $dt/dP > 0$ shows that the equilibrium Ni−O bond length is unusually compressible, signaling a double-well potential for the equilibrium bond length at the crossover from localized to itinerant electronic behavior. Above T_{IM}, strong coupling of electrons to optical phonons gives rise to "vibronic" states. Vibronic states in a phase with a dynamic CDW appears to be a characteristic feature of partially filled σ^* bands as we have argued elsewhere occurs in the mixed-valent manganese-oxide perovskites exhibiting a "colossal" negative magnetoresistance.[62−64]

References

(1) Shannon, R. D.; Prewitt, C. T. *Acta Crystallogr. B* **1969**, *25*, 725; **1970**, *26*, 1046.
(2) Goodenough, J. B.; Longo, J. M. *Landolt-Börnstein Tabellen*, New Series III/4a; Hellwege, K. H., Ed.; Springer-Verlag: Berlin, 1970; p 126.
(3) Radaelli, P. G.; Marezio, M.; Hwang, H. Y.; Cheong, S.-W. *J. Solid State Chem.* **1996**, *122*, 444.
(4) Goodenough, J. B.; Kafalas, J. A.; Longo, J. M. In *Preparative Methods in Solid State Chemistry*; Hagenmuller, P., Ed.; Academic: New York, 1972; Chapter 1.
(5) Longo, J. M.; Kafalas, J. A. *Mater. Res. Bull.* **1968**, *3*, 687.
(6) Goodenough, J. B. *Ferroelectrics* **1992**, *130*, 77.
(7) Arima, T.; Tokura, Y. *J. Phys. Soc. Jpn.* **1995**, *64*, 2488.
(8) Goodenough, J. B. In NATO "Davy" ASI, *Physics and Chemistry of Electrons and Ions in Condensed Matter*; Acrivos, J. V., Mott, N. F., Yoffee, A., Eds.; D. Reidel: Dordrecht, Holland, 1984; p 1.
(9) Greedan, J. E. *J. Less Common Metals* **1985**, *111*, 335.
(10) Tang, X.-X.; Manthiram, A.; Goodenough, J. B. *Physica C* **1989**, *161*, 574.
(11) Goodenough, J. B. *Prog. Solid State Chem.* **1971**, *5*, 145.
(12) Goodenough, J. B. *Mater. Res. Bull.* **1971**, *6*, 967.
(13) Zaanen, J.; Sawatzky, G. A.; Allan, J. W. *Phys. Rev. Lett.* **1985**, *55*, 418.
(14) Goodenough, J. B. *Ann. Chim. Fr.* **1982**, *7*, 489.
(15) (a) Takano, M.; Nakanishi, N.; Takeda, Y.; Naka, S.; Takada, T. *Mater. Res. Bull.* **1977**, *12*, 923. (b) Woodward, R., unpublished material.
(16) Rodríguez-Carvajal, J.; Hennion, M.; Moussa, F.; Moudden, A. H.; Pinsard, L.; Revcolevschi, A. *Phys. Rev.* **1998**, *B57*, R3189.
(17) Goodenough, J. B. *Phys. Rev.* **1955**, *100*, 564.
(18) (a) Señarís-Rodríguez, M. A.; Goodenough, J. B. *J. Solid State Chem.* **1995**, *116*, 323. (b) Yamaguchi, S.; Okimoto, Y.; Tokura, Y. *Phys. Rev.* **1997**, *B55*, R866.
(19) Bhide, V. G.; Rojoria, D. S.; Rao, G. R.; Rao, C. N. R. *Phys. Rev. B* **1972**, *6*, 1021.
(20) Asai, K.; Yoneda, A.; Yokokura, O.; Tranquada, J. M.; Shirane, G.; Kohn, K. *J. Phys. Soc. Jpn.* **1998**, *67*, 290.
(21) Goodenough, J. B. *Phys. Rev.* **1968**, *171*, 466.
(22) Borukhovich, A. S.; Bazuev, G. V.; Sveiken, G. P. *Sov. Phys. Solid State* **1973**, *15*, 1467; **1974**, *16*, 181.
(23) Borukhovich, A. S.; Bazuev, G. V.; Sveiken, G. P. *Sov. Phys. Solid State* **1974**, *16*, 191; **1976**, *18*, 1165.
(24) Shirakawa, N.; Ishikawa, M. *Jpn. J. Appl. Phys.* **1994**, *30*, L755.
(25) Mahajan, A. V.; Johnston, D. C.; Torgesen, D. R.; Borsa, F. *Phys. Rev. B* **1992**, *46*, 10966.
(26) Goodenough, J. B.; Nguyen, H. C. *C. R. Acad. Sci. Paris* **1994**, *319 Sér II*, 1285; *Phys. Rev. B* **1995**, *52*, 324.
(27) Ren, Y.; Palstra, T. T. M.; Khomskii, D. I.; Pellegrin, E.; Nugroho, A. A.; Menovsky, A. A.; Sawatzky, G. A. *Nature*, in press.
(28) Takeda, T.; Yamaguchi, Y.; Watanabe, H. *J. Phys. Soc. Jpn.* **1972**, *33*, 967.
(29) Goodenough, J. B.; Longo, J. M.; Kafalas, J. A. *Mater. Res. Bull.* **1968**, *3*, 471.
(30) Goodenough, J. B. *Czech. J. Phys.* **1967**, *17*, 304.
(31) Sparks, J. T.; Komoto, T. *Rev. Mod. Phys.* **1968**, *40*, 752.
(32) Morikawa, K.; Mizokawa, T.; Kobayashi, K.; Fujimori, A.; Eisaki, H.; Uchida, S.; Iga, F.; Nishihara, Y. *Phys. Rev. B* **1995**, *52*, 13711.
(33) Hubbard, J. *Proc. R. Soc. (London) A* **1963**, *276*, 238; **1964**, *277*, 237; **1964**, *281*, 401; **1965**, *285*, 542; **1966**, *81*, 100.
(34) Inoue, I. H.; Hase, I.; Aiura, Y.; Fujimori, A.; Haruyama, Y.; Maruyama, T.; Nishihara, Y. *Phys. Rev. Lett.* **1995**, *74*, 2539.
(35) Brinkman, W. F.; Rice, T. M. *Phys. Rev. B* **1970**, *2*, 4302.
(36) Zhou, J. S.; Goodenough, J. B. *Phys. Rev. B* **1996**, *54*, 13393.
(37) Fukushima, A.; Murata, K.; Morikawa, K.; Iga, F.; Kido, G.; Nishihara, Y. *Physica B* **1994**, *196*, 1161.
(38) Howson, M. A.; Gallagher, B. G. *Phys. Rev.* **1988**, *170*, 265.
(39) Johnson, M.; Mahan, G. D. *Phys. Rev. B* **1990**, *42*, 9350.
(40) Demazeau, G.; Parent, C.; Pouchard, M.; Hagenmuller, P. *Mater. Res. Bull.* **1972**, *7*, 913.
(41) Goodenough, J. B.; Mott, N. F.; Pouchard, M.; Demazeau, G.; Hagenmuller, P. *Mater. Res. Bull.* **1973**, *8*, 647.
(42) Zhou, J. S.; Archibald, W.; Goodenough, J. B. *Phys. Rev. B* **1998**, *57*, R2017.
(43) Papaconstantopoulos, D. P.; Boyer, L. L. In *Novel Superconductivity*; Wolf, S. A., Kresin, V. Z., Eds.; Plenum: New York, 1987; p 493.
(44) Okimoto, Y.; Katsufuji, T.; Okada, Y.; Arima, T.; Tokura, Y. *Phys. Rev. B* **1995**, *51*, 9581.
(45) Fujimori, A.; Hase, I.; Namatame, H.; Fujishima, Y.; Tokura, Y.; Eisaki, H.; Ochida, S.; Takegahara, K.; de Groot, F. M. F. *Phys. Rev. Lett.* **1992**, *69*, 1796.
(46) Goral, J. P.; Greedan, J. E.; MacLean, D. A. *J. Solid State Chem.* **1982**, *43*, 244.
(47) Goodenough, J. B. *J. Appl. Phys.* **1967**, *38*, 1054.
(48) MacLean, D. A.; Greedan, J. E. *Inorg. Chem.* **1981**, *20*, 1025.
(49) Katsufuji, T.; Taguchi, Y.; Tokura, Y. *Phys. Rev. B* **1997**, *56*, 10145.
(50) Turner, C. W.; Greedan, J. E. *J. Solid State Chem.* **1980**, *34*, 207.
(51) Kumagai, K.; Suzuki, T.; Taguchi, Y.; Okada, Y.; Fujishima, Y.; Tokura, Y. *Phys. Rev. B* **1993**, *48*, 7636.
(52) Reedyk, M.; Crandles, D. A.; Cardona, M.; Garrett, J. D.; Greedan, J. E. *Phys. Rev. B* **1997**, *55*, 1442.
(53) Okimoto, Y.; Katsufuji, T.; Okada, Y.; Arima, T.; Tokura, Y. *Phys. Rev. B* **1995**, *51*, 9581.
(54) Okada, Y.; Arima, T.; Tokura, Y.; Murayama, C.; Môri, N. *Phys. Rev. B* **1993**, *48*, 9677.
(55) Torrance, J. B.; Lacorre, P.; Nazzal, A. I.; Ansaldo, E. J.; Niedermayer, Ch. *Phys. Rev. B* **1992**, *45*, 8209.
(56) Medarde, M. L. *J. Phys., Cond. Matter* **1997**, *9*, 1681.
(57) García-Munoz, J. L.; Lacorre, P.; Cywinski, R. *Phys. Rev. B* **1995**, *51*, 15197.
(58) Rodríguez-Carvajal, J.; Rosenkranz, S.; Medarde, M.; Lacorre, P.; Ferandez-Díaz, M. T.; Fauth, F.; Tronnov, V. *Phys. Rev. B* **1998**, *57*, 456.
(59) Medarde, M.; Lacorre, P.; Conder, K.; Fauth, F.; Furrer, A. *Phys. Rev. Lett.* **1998**, *80*, 2397.
(60) Goodenough, J. B. *J. Solid State Chem.* **1996**, *127*, 126.
(61) Obradors, X.; Paulius, L. M.; Maple, M. B.; Torrance, J. B.; Nazzal, A. I.; Fontcuberta, J.; Granados, X. *Phys. Rev. B* **1993**, *47*, 12353. Canfield, P. C.; Thompson, J. D.; Cheong, S. W.; Rupp, L. W. *Phys. Rev. B* **1993**, *47*, 12357.
(62) Zhou, J. S.; Goodenough, J. B.; Asamitsu, A.; Tokura, Y. *Phys. Rev. Lett.* **1997**, *79*, 3234.
(63) Zhou, J. S.; Goodenough, J. B. *Phys. Rev. Lett.* **1998**, *80*, 2665.
(64) Goodenough, J. B.; Zhou, J. S. MRS Meeting, Boston, MA, Dec 1−5, 1997, Session V, Metallic Magnetic Oxides.

CM980276U